We are IntechOpen, the world's leading publisher of Open Access books
Built by scientists, for scientists

5,300
Open access books available

132,000
International authors and editors

160M
Downloads

Our authors are among the

154
Countries delivered to

TOP 1%
most cited scientists

12.2%
Contributors from top 500 universities

CLARIVATE ANALYTICS
BOOK CITATION INDEX
INDEXED

WEB OF SCIENCE™

Selection of our books indexed in the Book Citation Index
in Web of Science™ Core Collection (BKCI)

Interested in publishing with us?
Contact book.department@intechopen.com

1

Full-Field Optical Coherence Microscopy

Arnaud Dubois
Laboratoire Charles Fabry, UMR 8501
Institut d'Optique, CNRS, Univ Paris Sud 11
Palaiseau
France

1. Introduction

Optical coherence tomography (OCT) is a well-established optical imaging technique with micrometer-scale resolution. OCT is based on low-coherence interferometry to measure the amplitude of light backscattered by the sample being imaged [1-4]. The most significant impact of OCT is in ophthalmology for *in situ* examination of the pathologic changes of the retina [5-8] and measurement of the dimensions of the anterior chamber of the eye [9, 10]. OCT has also been established in a variety of other biomedical applications [11] and for material characterization [12, 13].

Optical Coherence Microscopy (OCM) is an OCT technique where high numerical aperture optics are used to achieve higher transverse spatial resolution. OCM generates *en face* rather than cross-sectional images with the transverse resolution of a microscope. Two general approaches for OCM have been reported to date. The first approach is based on the principle of point-scanning imaging developed in confocal microscopy [13-15]. The second approach involves full-field illumination and detection. Also sometimes termed Full-Field Optical Coherence Tomography (FF-OCT), Full-Field Optical Coherence Microscopy (FF-OCM) is an alternative technique to scanning OCM, based on white-light interference microscopy [16-18]. FF-OCM produces tomographic images in the *en face* orientation by arithmetic combination of interferometric images acquired with an area camera and by illuminating the whole field of view using a low-coherence light source [19-23]. The major interest of FF-OCM lies in its high imaging resolution in both transverse and axial directions, far higher than the resolution of conventional OCT, using a simple and robust experimental arrangement [24, 25]. Two extensions to the FF-OCM technique were recently proposed to provide additional information on the spectroscopic or birefringence properties of the sample being imaged [26, 27].

This chapter reports on the latest developments of the FF-OCM technology. Tomographic images can be acquired in two distinct spectral regions, centered at 750 nm and 1250 nm using two different cameras and a halogen lamp as illumination source. The principle of operation is explained and the system characteristics are reported in details, including the detection sensitivity and spatial resolution. Some limitations of the technique due to sample motion are studied theoretically and experimentally. A few images of biological samples are shown to illustrate the imaging capabilities.

2. The FF-OCM technique

2.1 Instrumentation

FF-OCM is typically based on the Linnik interference microscope configuration [19, 28]. The experimental arrangement is represented schematically in Figure 1. It consists of a Michelson interferometer with identical microscope objectives placed in both arms. Light is split into the reference and sample arms by a broadband beam splitter, with a variation of the ratio transmission/reflection less than 10% in the entire wavelength region of interest (700 - 1600 nm). The polished surface of an $Y_3Al_5O_{12}$ (YAG) crystal is placed in the reference arm of the Linnik interferometer in the focal plane of the microscope objective. This reference surface in contact with the immersion medium of the microscope objectives (water) provides a reflectivity $R_{ref} \sim 2.5\%$. A 100 W tungsten halogen lamp is incorporated in a Köhler system to provide uniform illumination of the microscope objective fields with spatially incoherent broadband light. The interferometric images delivered by the Linnik microscope are projected onto two camera arrays, a silicon-based CCD camera (Model 1M15 from Dalsa, 15 Hz, 1024×1024 pixels, 12 bits, called "Si camera" in this chapter) with a maximal sensitivity at the wavelength of ~ 750 nm and an InGaAs area scan camera (Model SU320MS from Sensors Unlimited, 25 Hz, 320×256 pixels, 12 bits, called here "InGaAs camera") with a maximal sensitivity at ~ 1300 nm. 2×2 pixel binning is applied with the Si camera to increase the dynamic range of the detection, and hence the detection sensitivity as will be explained later. This 2×2 pixel binning is performed numerically after each image acquisition. A dichroic mirror with high reflectivity (>98%) in the 650-950 nm band and high transmission (>85%) in the 1100 -1500 nm is used to separate both spectral bands before detection. Water-immersion microscope objectives (Olympus, 10×, numerical aperture of 0.3) are used to minimize dispersion mismatch in the interferometer arms as the imaging depth in the sample increases, and to reduce light reflection from the sample surface. The length of the interferometer reference arm can be varied without modifying the focus on the reference surface by translating together all the elements placed in this arm using a motorized axial translation stage. Another motorized axial translation stage is used to translate the objective in the sample arm so that the focus plane and the coherence plane always match. This adjustment is performed automatically by entering the proper value of the refractive index of the sample in the graphical interface of the FF-OCM system software.

2.2 Principle of operation

The tomographic signal in FF-OCM is extracted by calculating the amplitude of the interference signal using the principle of phase-shifting interferometry [17-21]. We use here a two-step phase-shifting method, *i.e.* The tomographic image is obtained by combination of only two interferometric images (two frames), the phase being shifted between each of them [25, 29].

The reference surface is attached to a piezoelectric actuator (PZT) to make it oscillate between two positions distant of a quarter of the illumination center wavelength divided by the refractive index of water, *i.e.* 0.14 µm when the Si camera is used and 0.23 µm when the InGaAs camera is used. The change of position of the reference mirror thus generates a phase-shift in the interferometer of about π. An adjustable number N of pairs of phase-
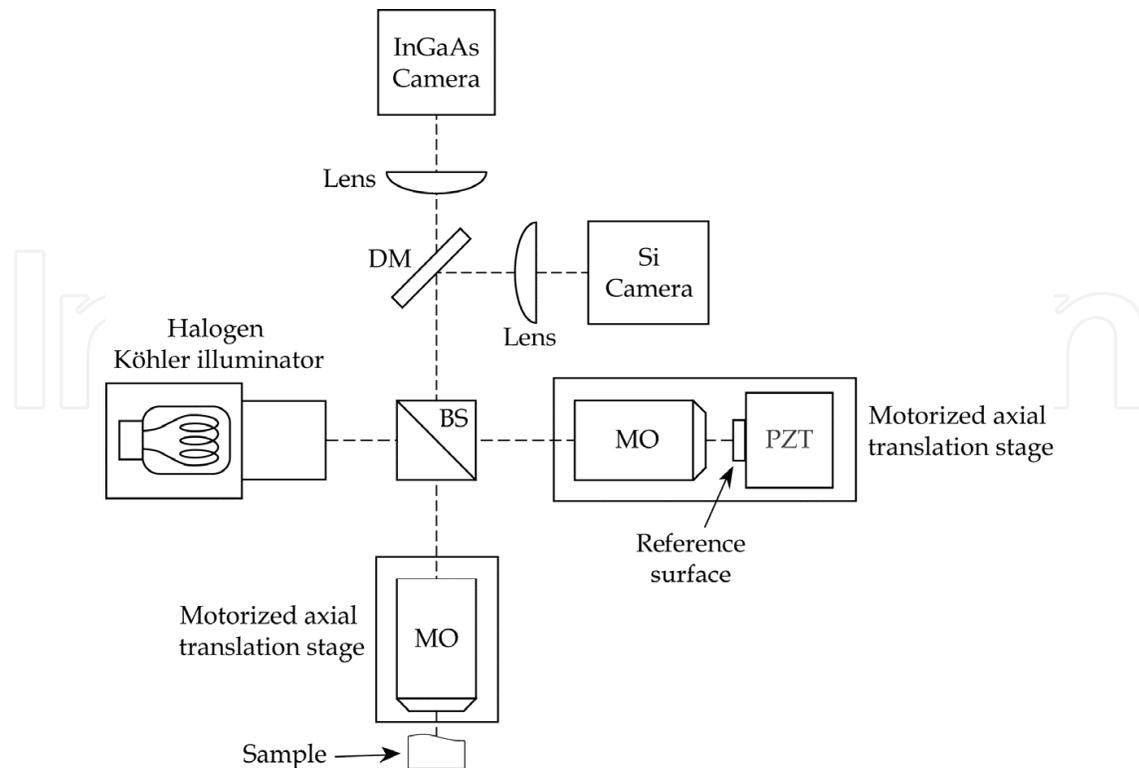
Fig. 1. Schematic of the experimental set-up of FF-OCM. MO, microscope objective; BS, beam-splitter cube; DM, dichroic mirror; PZT, piezoelectric actuator.

opposed interferometric images can thus be acquired by both cameras. The images corresponding to the same phase are summed up, which yields a single pair of frames that can be written as

$$E_1 = \left\{ \sum_{n=0}^{N-1} \left[\int_{2nT}^{(2n+1)T} I_1 dt \right] \right\}, \quad E_2 = \left\{ \sum_{n=0}^{N-1} \left[\int_{(2n+1)T}^{(2n+2)T} I_2 dt \right] \right\}, \tag{1}$$

where T is the integration time of the camera in use. The irradiance (or intensity) I_1 and I_2 received by each pixels of the camera are (K being a proportionality coefficient):

$$\begin{cases} I_1(x,y,z) = K\left\{ R_{sample}(x,y,z) + R_{ref} + 2\gamma(z)\sqrt{R_{sample}(x,y,z)R_{ref}} \cos[\phi(x,y,z)] \right\}, \\ I_2(x,y,z) = K\left\{ R_{sample}(x,y,z) + R_{ref} + 2\gamma(z)\sqrt{R_{sample}(x,y,z)R_{ref}} \cos[\phi(x,y,z) + \pi] \right\}. \end{cases} \tag{2}$$

The squared difference of the pair of accumulated frames,

$$\left(E_1 - E_2\right)^2 = 16K^2N^2T^2R_{ref}\gamma^2(z)R_{sample}(x,y,z)\cos^2[\phi(x,y,z)], \tag{3}$$

is proportional to the three-dimensional reflectivity distribution of the sample $R_{sample}(x,y,z)$ multiplied by the coherence function $\gamma^2(z)$. It corresponds to an image of the reflecting or backscattering structures of the sample located in a slice, perpendicular to the optical axis, of width equal to the coherence length (width of the coherence function). This image corresponds to an *en face* tomographic image of the sample at depth z.

One can see from Eq. (3) that the tomographic image contains a term with the optical phase ϕ. A combination of more than two frames would be required to separate the amplitude and the phase [19-23]. However, due to the size and distribution of the structures in most samples being imaged, interference fringes are generally not visible in the tomographic images. We have adopted a method with only two frames to maximize the processing speed. A tomographic image can be produced at a maximum rate equal to half the camera frame rate, *i.e.* 7.5 Hz with the Si camera and 12.5 Hz with the InGaAs camera. However, in practice it is necessary to accumulate several interferometric images to improve the detection sensitivity, as will be shown later. The tomographic images are then produced at a frequency on the order of 1 Hz.

3. System characteristics

3.1 Detection sensitivity

Detection sensitivity is a key system parameter in OCT that affects the imaging contrast and penetration depth. Several possible sources of noise have to be considered for the determination of the detection sensitivity in FF-OCM. In addition to the shot noise induced by the fundamental photon noise, other kinds of noise originating from the cameras may not be negligible such as the electrical noise, including the read out noise and the dark noise. Assuming the well of the camera pixels to be full upon maximal illumination, and neglecting the relative intensity noise, it has been shown [19, 21, 22, 30] that the minimal detectable reflectivity can be written as

$$R_{min} = \frac{\left(R_{inc} + R_{ref}\right)^2}{4NR_{ref}} \left(\frac{1}{\xi_{sat}} + \frac{\eta^2}{\xi_{sat}^2}\right). \tag{4}$$

The parameter ξ_{sat} denotes the full-well-capacity of the camera pixels, and η the noise-equivalent electrons representing the total electrical noise. One can see from Eq. (4) that increasing the full-well-capacity decreases the value of R_{min} (*i.e.* the sensitivity is improved). The full-well-capacity can be increased by custom adjustment of the camera gain setting. However, since increasing the gain also generally causes the electrical noise of the camera to increase in the same proportion (η and ξ_{sat} are proportional) [22, 30], one can see from Eq. (4) that the sensitivity is limited. Besides, a larger full-well-capacity requires a more powerful light source, which constitutes a technological limit. At last, the illumination power that can be tolerated by the sample is also limited, especially when the sample is a biological medium.

One can also see from Eq. (4) that the detection sensitivity depends on the amount of incoherent light, through the parameter R_{inc}. This parameter represents the proportion of incoherent light (light that does not interfere), resulting essentially from backscattering and backreflection by structures within the sample present outside the coherence volume. The detection sensitivity is maximized (R_{min} is minimized) when R_{inc} is minimal. For that purpose, all the optical components are antireflection coated and the beam-splitter is slightly tilted to avoid specular reflections. We have measured that the incoherent light coming from the setup without sample represents a reflectivity of $R_{inc} \sim 0.5\%$. When a biological sample is imaged, the reflection on the sample surface is minimized by index matching, achieved by using water-immersion objectives. The incoherent light coming from typical biological

samples and collected by the microscope objective does not exceed a few percents. The reference mirror reflectivity R_{ref} has also an influence on the detection sensitivity. By calculating the derivative of Eq. (4) with respect to R_{ref}, one can easily establish that the optimal value of R_{ref} is reached when $R_{ref} = R_{inc}$, which is approximately the case in practice ($R_{ref} = 2.5\%$).

At last, Equation (4) indicates that the detection sensitivity can be improved with image accumulation (parameter N). The benefit of image accumulation is illustrated in Figure 2. A mouse embryo embedded in an agarose gel was imaged with different accumulation numbers. The signal-to-noise ratio in the images is clearly improved when the accumulation number is increased. Since accumulating images increases the acquisition time, this way of improving the detection sensitivity is however limited if the sample is likely to move during this time. *In vivo* imaging, in particular, may be incompatible with image accumulation. A study of artifacts in FF-OCM induced by sample motion will be presented in section 4.
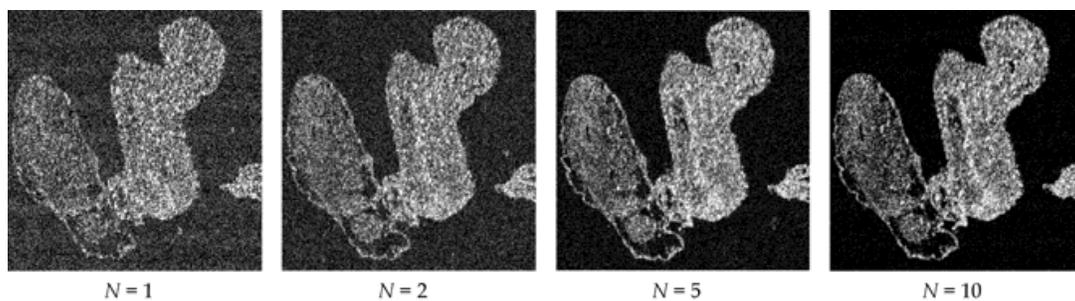

Fig. 2. FF-OCM images of a mouse embryo, *in vitro*, for different numbers N of accumulated images, using the Si camera.

Measurements of the detection sensitivity were carried out. A glass plate was used as low reflectivity sample. The results are summarized in Figure 3 showing the value of R_{min} in logarithmic scale as a function of the number N of images accumulated by each camera. One can see that a detection sensitivity on the order of - 90 dB is achievable with an accumulation of 10 images using the Si camera and 30 images using the InGaAs camera, which represents an acquisition time of ~ 1 s and 2 s for the Si and InGaAs cameras respectively. The straight lines correspond to the sensitivity calculated with Eq. (4) by taking $R_{ref} = 2.5\%$ and $R_{inc} = 0.5\%$ for both cameras. For the Si camera, we considered a full-well-capacity $\xi_{sat} = 1 \times 10^6$ (with 2×2 pixel binning) and a noise-equivalent electrons $\eta = 0$; for the InGaAs camera, these parameters were $\xi_{sat} \sim 8 \times 10^5$ and $\eta = 400$. The theory is in agreement with the experiment for the Si camera, whereas a discrepancy is observed for the InGaAs camera, which may be explained by the presence of additional noise not taken into account in the model and (or) optical aberrations of the microscope objectives at these large wavelengths.

3.2 Wavelength and imaging penetration depth

Detection sensitivity affects the imaging contrast and therefore the imaging penetration depth. For a given sensitivity, however, the imaging penetration depth may depend on the illumination wavelength. The propagation of light in biological media is affected by two wavelength-dependant attenuation mechanisms: scattering and absorption. Scattering is due to the presence of structures within the sample creating refractive index heterogeneities.
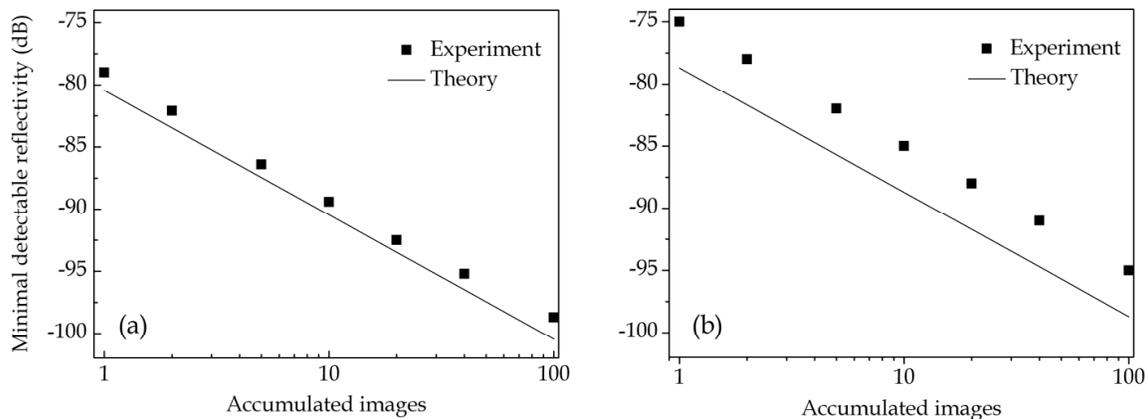
Fig. 3. Detection sensitivity of FF-OCM as a function of image accumulation using the Si camera (a) and the InGaAs camera (b).

The intensity of light scattered by these particles depends strongly on their size and nature. A general tendency of scattering is a decrease of its intensity when wavelength increases [31, 32]. Absorption of light in biological media is dominated by the absorption water. This absorption is minimal at the wavelength of ~ 500 nm and globally increases with wavelength [33]. The optimal wavelength to maximize the OCT imaging penetration depth results from the best trade-off between scattering and absorption. Previous works have shown better imaging penetration depth in highly scattering tissues for OCT operating in the 1300 nm wavelength region compared to 800 nm [34, 35]. Similar results were also observed in FF-OCM [36].

The effect of scattering on the imaging penetration depth was studied in FF-OCM by imaging a highly contrasted sample placed behind a scattering medium. We considered as sample a mask for photolithography made of metallic structures deposited on a glass substrate. The scattering medium was a 3 mm-thick layer of 4% Intralipid solution commonly used to simulate scattering by biological media [37, 38]. Figures 4 shows *en face* tomographic images in the plane of the glass surface through the scattering layer, obtained with both cameras with the same detection sensitivity (by adjustement of the accumulation number *N*). The metallic structures of the sample are perfectly revealed by using the InGaAs camera, whereas they are almost completely obscured by the scattering medium when imaged with the Si camera because of much stronger scattering.

When a biological sample is imaged, however, the situation is quite different because the intensity of light backscattered by the structures inside the sample is also wavelength-dependent, which was not the case with the sample considered here. Reduced scattering permits longer propagation distances of useful light, but on the other hand weakens the signal resulting from backscattering by small particles.

3.3 Axial resolution

In conventional OCT, the axial response is governed by the coherence function $\gamma(z)$ equal to the Fourier transform of the effective source power spectrum [3]. Since this technique produces cross-sectional images (B scans), a large depth of focus is generally required, which imposes
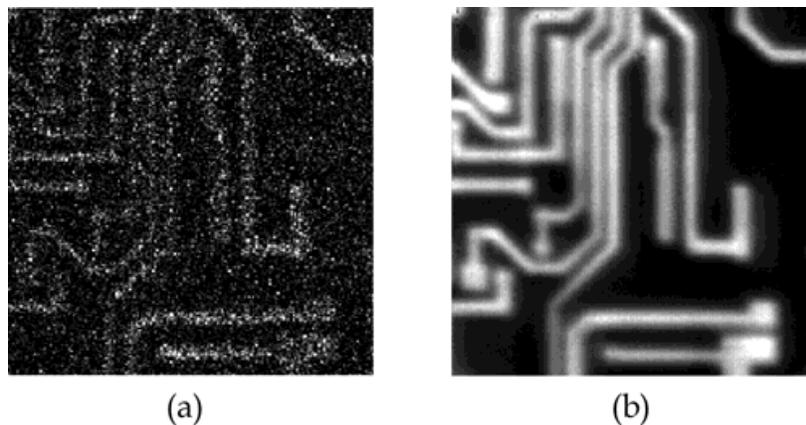
Fig. 4. FF-OCM images, using the Si camera (a) and the InGaAs camera (b), of a mask for photolithography through a layer of 3 mm thick Intralipid solution.

the use of low numerical aperture optics. FF-OCM acquires images in the *en face* orientation like a conventional microscope, which permits the use of microscope objectives of relatively high numerical aperture (*NA*). In that case, the axial response is determined not only by the coherence function but also by the depth of focus. Assuming a Gaussian-shaped effective spectrum, the theoretical axial resolution of FF-OCM can be defined, at the surface of the sample, as [19]

$$\Delta z = \left[\frac{NA^2}{n_{im}\lambda} + \frac{n_{im}\pi}{2\ln 2}\left(\frac{\Delta\lambda}{\lambda^2}\right) \right]^{-1},$$

(5)

where n_{im} is the refractive index of the objective immersion medium, λ the center wavelength and $\Delta\lambda$ the full-width at half maximun (FWHM) of the effective optical spectrum given by the product of the light source, the spectral transmission of the system optical components including the sample and the immersion medium themselves, and the spectral response of the camera in use.

The set-up described here is characterized by a relatively modest numerical aperture (*NA* = 0.3) and a very broadband light source (halogen lamp); the axial resolution is then essentially imposed by the temporal coherence in both detection bands. The theoretical axial resolution with the Si camera was calculated to be equal to 0.75 μm (λ = 750 nm, $\Delta\lambda$ = 250 nm). With the InGaAs camera, the absorption by the immersion medium (water) limits the effective spectral range above 1400 nm (although the spectral response of the InGaAs camera extends to 1700 nm). Considering an effective spectrum of width $\Delta\lambda$ = 400 nm centered at λ = 1250 nm, the theoretical axial resolution is 1.3 μm. The use of dry microscope objectives would yield a theoretical axial resolution of 0.9 μm because of a broader effective spectrum. However, it would severely degrade as the imaging depth in the sample increases because of dispersion mismatch in the interferometer [24]. From a certain depth, the axial resolution with dry objectives would even be weaker than the one obtained with immersion objectives. A configuration with water-immersion objectives was therefore favored to minimize dispersion mismatch and also reduce the reflection of light at the surface of the sample. The degradation of axial resolution with depth is then weak, but cannot be totally avoided because of refractive index inhomogeneities in the sample that are at the origin of the image contrast.

We have measured the interferogram response of our FF-OCM system with both cameras using a glass plate as sample (see Figure 5). The coherence function that comprises the interference fringes looks Gaussian with the Si camera. In comparison with broadband sources used in ultrahigh-resolution OCT, such as ultra-short femtosecond lasers or supercontinuum fiber lasers [39, 40], a thermal light source provides a smoother spectrum that does not contain spikes or emission lines that could cause side lobes in the coherence function and create artifacts in the images. The coherence function measured with the InGaAs camera, in contrast with the Si camera, has some wings resulting from dips in the effective spectrum due to water absorption [29, 33, 36]. The experimental FWHM of the coherence function was found to be 0.8 μm for the Si camera and 1.5 μm for the InGaAs camera, close to the theoretical values.
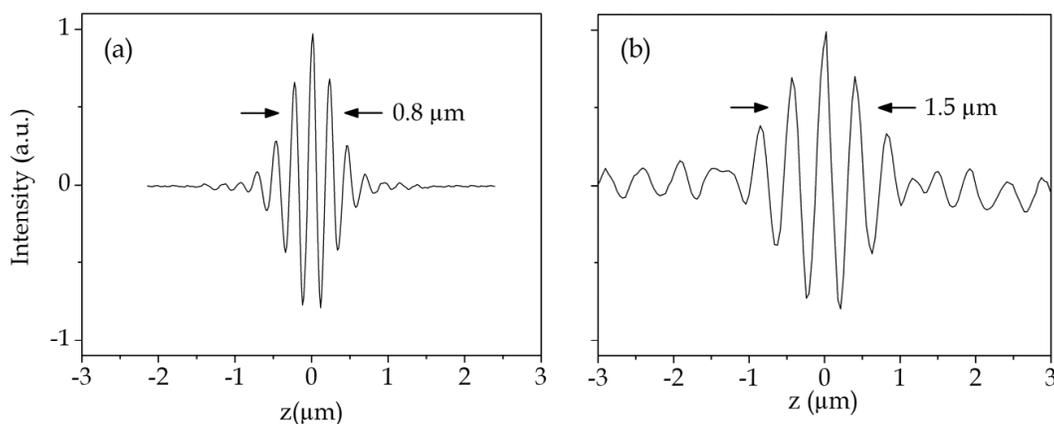
Fig. 5. Interferogram response measured with the Si camera (a) and the InGaAs camera (b). The width (FWHM) of the interferogram envelope is indicated.

3.4 Transverse resolution

The transverse resolution of an imaging system is commonly defined as the width of the transverse point-spread function (TPSF). When the optical system is diffraction-limited (*i.e.* bare of any optical aberration), the TPSF is the well-known Airy function. In that case an expression of the theoretical transverse resolution is

$$\Delta r = \frac{\lambda}{2NA}. \tag{6}$$

The previous equation gives theoretical diffraction-limited resolutions of 1.3 μm and 2.1 μm for the FF-OCM system using the Si camera and the InGaAs camera respectively, when microscope objective with numerical aperture of $NA = 0.3$ are employed.

We have measured the FWHM of the experimental TPSF of our FF-OCM system indirectly by recording an intensity profile across a cleaved mirror. Theoretically, the response is the convolution of a perfect edge and the experimental TPSF and a rectangular function that simulates the image sampling by the camera pixels. We considered here a Gaussian-shaped TPSF. Simulations were carried out to fit the experimental data by adjusting the TPSF width. The results are presented in Table 1. The experimental transverse resolutions are 1.4 μm and

2.7 μm for the Si and InGaAs cameras respectively. The degradation between experimental and theoretical transverse resolution for the InGaAs setup is attributed to optical aberrations of the microscope objectives that are not optimized in the spectral region detected by the InGaAs camera. Their transmission drops from 81% at 800 nm to 59% at 1200 nm. Moreover, optical aberrations are not well corrected, which degrades the image contrast and resolution.

	Theoretical	Experimental
Δr (μm) Si camera	1.3	1.4
Δr (μm) InGaAs camera	2.1	2.7

Table 1. Transverse resolution Δr associated to each camera. Microscope objectives with a numerical aperture of 0.3 were employed.

4. Sample motion artifacts

Artifacts resulting from motion of the sample being imaged occur in nearly all biomedical imaging modalities [41-43], including OCT [44]. Great efforts have been made to eliminate these artifacts since they may severely degrade the image quality and cause misinterpretations. In this section, we propose a theoretical and experimental study of motion artifacts in FF-OCM [45]. We distinguish the effect of signal loss and the effect of spurious signal apparition.

4.1 Loss of signal

Optical systems based on interferometry are generally very sensitive to vibrations. Due to the short wavelength of optical waves, path length variations of only a few tens of nanometers may generate significant phase changes, which may cause a blurring of the detected interference signal if the integration time of the detector is not short enough.

In FF-OCM, sample motions along the axial direction generate changes of the optical path length of the interferometer sample arm. In contrast, motions along the transverse direction do not change the optical path length. Assuming monochromatic illumination at wavelength λ and axial displacement of the sample at constant speed v, the optical phase in the interferometer varies linearly with time as

$$\phi(t) = \frac{4\pi n}{\lambda} vt, \tag{7}$$

where n denotes the refractive index of the immersion medium. The tomographic image obtained from the squared difference of two phase-opposed accumulated interferometric images can then be written as

$$(E_1 - E_2)^2 = 4K^2\gamma^2 R_{sample}R_{ref}\left\{\sum_{n=0}^{N-1}\left[\int_{2nT}^{(2n+2)T}\cos\left(\frac{4\pi n}{\lambda}vt\right)dt\right]\right\}^2$$

$$= 16K^2\gamma^2 N^2 T^2 R_{sample}R_{ref} \times B(v), \tag{8}$$

where

$$B(v) = \left[\frac{\sin\left(\frac{8\pi n}{\lambda} vNT \right)}{\left(\frac{8\pi n}{\lambda} vNT \right)} \right]^2 . \tag{9}$$

One can see from the previous equations that the variation of the amplitude of the tomographic signal with axial speed of the sample is described by the function $B(v)$. One can define the maximal tolerable speed v_{max} as the first zero of the function $B(v)$, *i.e.*

$$v_{\max} = \frac{\lambda}{8nNT} . \tag{10}$$

The maximal tolerable speed corresponds to a displacement of the sample of $\lambda/4n$ during the total acquisition time (equal to $2NT$), which corresponds to an optical path length change of $\lambda/2n$ or a phase change of π. Theoretical values of v_{max} calculated with Eq. (10) are reported in Table 2 for both cameras for different accumulation numbers N.

Accumulations N	1	2	5	10	20
$v_{\max}$ (μm/s) Si camera	1.05	0.53	0.21	0.10	0.05
$v_{\max}$ (μm/s) InGaAs camera	2.94	1.47	0.59	0.29	0.15

Table 2. Maximal tolerable axial speed of the sample for both cameras. These theoretical values are obtained by computation of Eq. (10) with [T = 67 ms, λ = 750 nm] for the Si camera , and [T = 40 ms, λ = 1250 nm] for the InGaAs camera. The immersion medium is water (n = 1.33).

We also performed measurements of the amplitude of the tomographic signal as a function of axial speed of the sample. For this experiment, a mirror mounted on a piezoelectric actuator was used as a sample. The position of the mirror at zero voltage applied to the piezoelectric coincided with the focal plane of the microscope objective. Figure 6 shows how the amplitude of the tomographic signal decreases as a function of the mirror axial speed for accumulations of 1, 2 and 3 pairs of images. A very good agreement is observed between the experimental data and the theoretical curves based on Eq. (9).

In conclusion, the present FF-OCM technique is not appropriate for imaging samples whose axial motion is faster than 1μm/s typically. *In vivo* imaging may therefore be difficult with this technique. For example the speed of blood flow is a few hundreds of μm/s. Physiological motions such as the cardiac motion may even reach 100 mm/s. For these kinds of applications, a shorter acquisition time is definitely required. High speed systems have been proposed [45-49], making *in vivo* imaging possible. However, the detection sensitivity of these systems is quite low. A real benefit would be to use a camera such that the ratio ξ_{sat}/T is larger. The reduction of acquisition time, without loss of sensitivity, would then be approximately inversely proportional to the increase of this ratio, provided that the
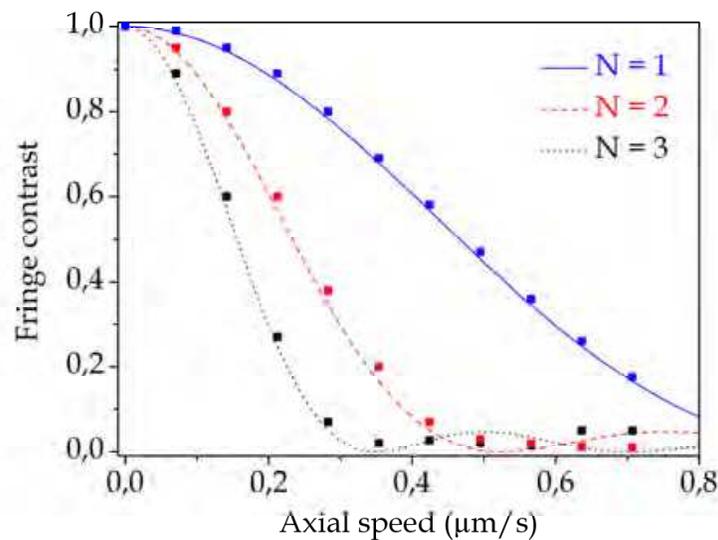
Fig. 6. Fringe contrast as a function of axial speed of the sample using the Si camera, for different accumulation numbers N. Comparison between experimental data (squares) and theory (lines).

brightness of the light source can be sufficiently increased to fill the pixel wells and that the sample can tolerate a higher illumination power.

4.2 Spurious signal

FF-OCM images are obtained by combination of interferometric images (frames) acquired sequentially in time. The tomographic signal in FF-OCM is generated by the variation of the interferometric signal amplitude induced by the phase-shift introduced between these successive frames by the reference surface oscillation. However, the intensity of light upon each pixel of the cameras may also vary if the backscattering structures of the sample move transversally. This variation of intensity generates a spurious signal, which superimposes on the tomographic signal and may cause misinterpretations of the tomographic images. Axial motion of the sample has much less influence on this spurious signal, since it only causes a defocus, which does not change significantly the intensity of light received by each pixel.

We performed numerical simulations to evaluate the effect of continuous transverse motion of the sample during the integration time of the camera. We considered as a sample a particle smaller than the optical wavelength. The image of this particle on the camera array detector is assumed to be an Airy pattern of dimension determined by the center wavelength and the numerical aperture of the microscope objective (see Eq. (6)), and also the magnification of the complete imaging system. The principle of the simulation is to calculate the variation of intensity on the CCD pixels induced by a transverse displacement of the particle. We consider that the motion of the particle becomes visible when the resulting intensity variation is greater than the minimal detectable reflectivity R_{min} given by Eq. (4). Figure 7 shows the evolution of the maximal tolerable transverse speed of the particle as a function of its reflectivity for different accumulation numbers. For example, for a particle with equivalent reflectivity of 10^{-5} and an accumulation of 5 pairs of images,

transverse motion at speed lower than ~ 100 μm/s is not visible. The effect of transverse motion is clearly less severe than the effect of axial motion. Artifacts resulting from transverse motion can even be completely removed if the frames are acquired simultaneously and not sequentially in time. For that purpose, instantaneous phase-shifting interferometry was successfully applied in FF-OCM, at the price of an increase in system complexity, calibration and cost [45, 46, 48, 50].
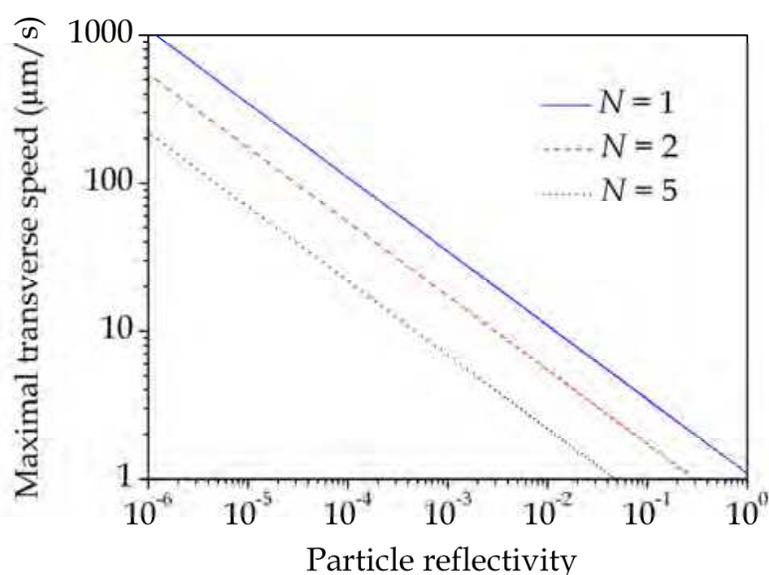

Fig. 7. Theoretical maximal transverse speed of a particle versus its reflectivity, using the Si camera. The calculations were done for different accumulation numbers N.

5. Illustration of imaging capabilities

The imaging capability of FF-OCM in the biomedical field has been extensively reported. Cellular-level resolution images of various ophthalmic tissues [51], embryos and plants [24, 25, 52, 53] have been published. A few other examples obtained with the FF-OCM technique described in this chapter are presented in this section. All the biological samples considered here are biopsy tissues. They were imaged *ex vivo*, with a drop of physiological serum inserted between the microscope objective and the samples. The microscope objectives, with numerical aperture of 0.3, had a working distance of 3.3 mm. The experimental procedure consisted of acquiring a stack of tomographic images at successive depths in constant steps of 0.7 μm. Sections in arbitrary orientations could then be computed for display. All the images are presented in logarithmic scale using different colormaps.

Cross-sectional images of rabbit cornea, obtained with both cameras, are presented in Figure 8. Two layers corresponding to the choroid and the sclera of the cornea can be distinguished. As expected, deeper structures can be imaged by using the InGaAs camera. The spatial resolution, however, is better at shorter wavelengths using the Si camera.

Another example of tissue imaged with FF-OCM is presented in Figure 9. The sample consisted of a piece of cartilage removed from a pig shoulder. Two sections in orthogonal orientations (cross-sectional and *en face*) show the distribution of isogenous groups within

the cartilage tissue. The territorial and interterritorial matrices are clearly visible. Within the cartilage matrix, cells are located in spaces called lacunae filled by chondrocyte. In *ex vivo* cartilage, however, the cells frequently shrink and even fall out. Only empty spaces, where the chondrocytes once sat, are probably observed here.
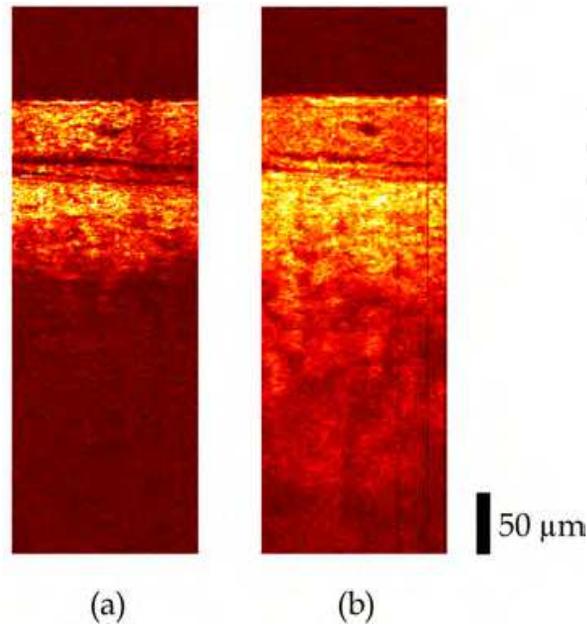

Fig. 8. FF-OCM images of rabbit cornea, *in vitro*, obtained with the Si camera (a) and the InGaAs camera (b). These cross-sectional (XZ) tomographic images are computed from a stack of 800 *en face* tomographic images.
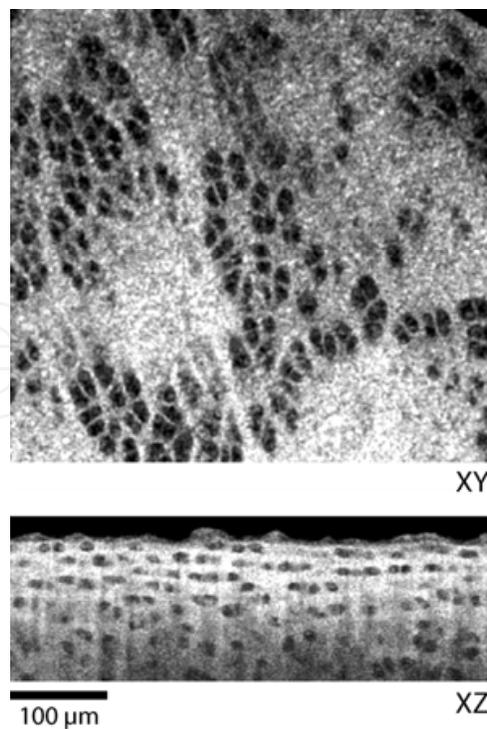
Fig. 9. FF-OCM images, in orthogonal views, of pig cartilage from a biopsy conducted in the region of the shoulder.

A cross-sectional image of human skin obtained with FF-OCM is shown in Figure 10. The skin sample was imaged immediately after a punch biopsy performed in the region of the forearm. The cross-sectional view allows for the visualization of different layers. The epidermis and dermis layers, in particular, can be clearly distinguished. Theses layers are separated by the papillary region. The reticular region in the dermal layer contains small blood vessels, lymph and nerves, fine collagen and elastic fibers. The epidermis layer is composed of several thinner layers including the stratum corneum, the stratum granulosum, the stratum spinosum and the stratum basale.
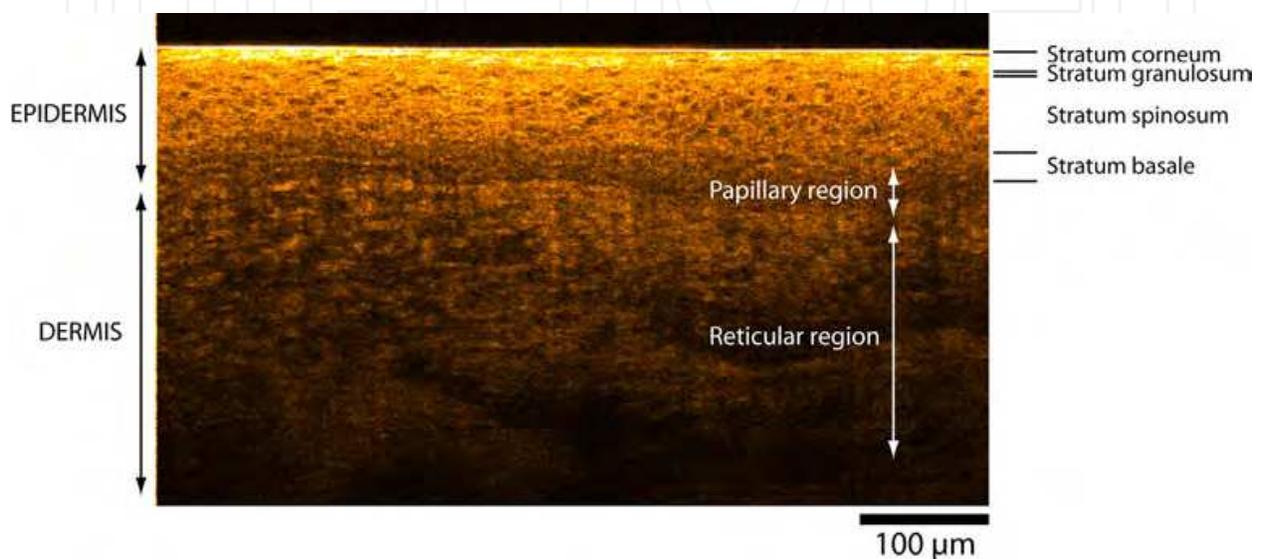
Fig. 10. FF-OCM cross-sectional image of human skin in the forearm region.

6. Conclusion

FF-OCM is an alternative technique to conventional scanning OCM that provides ultrahigh-resolution images using a simple tungsten-halogen lamp, instead of a sophisticated laser-based source. We have demonstrated here a system capable of imaging in two distinct spectral regions, which is relevant depending on whether one wish to favor the imaging penetration depth or the spatial resolution. With a spatial resolution approaching that of microscopy, this technology has the potential to replace conventional methods used for histology. *In vivo* imaging is still difficult with FF-OCM because of the appearance of artifacts resulting from sample motion. With the constant advances in the technologies of cameras and light sources, one can reasonably think that the acquisition speed of FF-OCM will be considerably improved in a near future. FF-OCM would then become a powerful tool for ultrahigh-resolution *in vivo* imaging without any contrast agent, making *in situ* examination possible without the need for histological processing of tissues.

7. Acknowledgment

8. References

[1] Huang, D.; Swanson, E.A.; Lin, C.P.; Schuman, J.S.; Stinson, W.G.; Chang, W.; Hee, M.R.; Flotte, T.; Gregory, K.; Puliafito, C.A. & Fujimoto J.G. (1991). Optical Coherence Tomography. *Science*, Vol.254, pp. 1178-1181

[2] Fujimoto, J.G.; Brezinski, M.E.; Tearney, G.J.; Boppart, S.A.; Bouma, B.E.; Hee, M.R.; Southern, J.F. & Swanson E.A. (1995). Optical biopsy and imaging using optical coherence tomography. *Nature Medicine*, Vol.1, pp. 970-972

[3] Fercher, A.F. (1996). Optical coherence tomography. *Journal of Biomedical Optics*, Vol.1, pp. 157-173

[4] Tearney, G.J.; Bouma, B.E.; Boppart, S.A.; Golubovic, B.; Swanson, E.A. & Fujimoto, J.G. (1996). Rapid acquisition of in-vivo biological images by use of optical coherence tomography. *Optics Letters*, Vol.21, pp. 1408-1410

[5] Swanson, E.A.; Izatt, J.A.; Hee, M.R.; Huang, D.; Lin, C.P.; Schuman, J.S.; Puliafito, C.A.; Fujimoto, J.G. (1993). In-vivo retinal imaging by optical coherence tomography. *Optics Letters*, Vol.18, pp. 1864-1866

[6] Wojtkowski, M.; Leitgeb, R.; Kowalczyk, A.; Bajraszewski, T. & Fercher, A.F. (2002). In-vivo human retinal imaging by Fourier domain optical coherence tomography. *Journal of Biomedical Optics*, Vol.7, pp. 457-463

[7] Hitzenberger, C.K.; Trost, P.; Lo, P.W. & Zhou, Q. (2003). Three-dimensional imaging of the human retina by high-speed optical coherence tomography, *Optics Express*, Vol.11, pp. 2753-2761

[8] Nassif, N.; Cense, B.; Park, B.H.; Yun, S.H.; Chen, T.C.; Bouma, B.E.; Tearney G.J., & de Boer, J.F. (2004). In-vivo human retinal imaging by ultrahigh-speed spectral domain optical coherence tomography. *Optics Letters*, Vol.29, pp. 480-482

[9] Izatt, J.A.; Hee, M.R.; Swanson, E.A.; Lin, C.P.; Huang, D.; Schuman, J.S.; Puliafito C.A. & Fujimoto, J.G. (1994). Micrometer-scale resolution imaging of the anterior eye in vivo with optical coherence tomography, *Archives of Ophthalmology*, Vol.112, pp. 1584-1589

[10] Trefford, S. & Desmond, F. (2008). Optical Coherence Tomography of the Anterior Segment. *Ocular Surface*, Vol.6, pp. 117-127

[11] Fujimoto, J.G. (2003). Optical coherence tomography for ultrahigh resolution in vivo imaging. *Nature Biotechnology*, Vol. 21, pp. 1361-1367

[12] Desmond, C.A.; Stenger, J.; Gorczynska, I; Lie, H.; Teri, H.; Spronk, R.; Wolohojian, S., Khandekar, N.; Jiang, J.Y.; Barry, S.; Cable, A.E.; Huber, R. & Fujimoto J.G. (2007). Comparison of three-dimensional optical coherence tomography and high resolution photography for art conservation studies. *Optics Express*, Vol.15, pp. 15972-15986

[13] Wiesauer, K.; Pircher, M.; Götzinger, E.; Bauer, S.; Engelke, R.; Ahrens, G.; Grützner, G.; Hitzenberger, C. & Stifter, D. (2005). En face scanning optical coherence tomography with ultra-high resolution for material investigation. *Optics Express*, Vol.13, pp. 1015-1024

[14] Izatt, J.A.; Hee, M.R.; Owen, G.M.; Swanson, E.A. & Fujimoto J.G. (1994). Optical coherence microscopy in scattering media. *Optics Letters*, Vol.19, pp. 590-592

[15] Podoleanu, A.G.; Dobre, G.M. & Jackson, D.A. (1998). En face coherence imaging using galvanometer scanner modulation. *Optics Letters*, Vol.23, pp. 147-149

[16] Caber, P.J. (1993). Interferometric profiler for rough surfaces. *Applied Optics*, Vol.32, pp. 3438-3441

[17] Larkin, K.G. (1996). Efficient nonlinear algorithm for envelope detection in white light interferometry, *Journal of the Optical Society of America A*, Vol.13, pp. 832-843

[18] Kino, G.S. & Chim, S.C. (1990). Mirau correlation microscope, *Applied Optics*, Vol. 29, pp. 3775-3783

[19] Dubois, A.; Vabre, L.; Boccara, A.C. & Beaurepaire, E. (2002). High-resolution full-field optical coherence tomography with a Linnik microscope. *Applied Optics*, Vol.41, pp. 805-812

[20] Vabre, L.; Dubois, A. & Boccara, A.C. (2002). Thermal-light full-field optical coherence tomography. *Optics Letters*, Vol.27, pp. 530-532

[21] Laude, B.; De Martino, A.; Drévillon, B.; Benattar, L. & Schwartz, L. (2002). Full-field optical coherence tomography with thermal light. *Applied Optics*, Vol. 41, pp. 6637-6645

[22] Oh, W.-Y.; Bouma, B. E.; Iftimia, N.; Yelin, R. & Tearney, G.J. (2006). Spectrally-modulated full-field optical coherence microscopy for ultrahigh-resolution endoscopic imaging. *Optics Express*, Vol.14, pp. 8675-8684

[23] Sato, M.; Nagata, T.; Niizuma, T.; Neagu, L.; Dabu, R. & Watanabe, Y. (2007). Quadrature fringes wide-field optical coherence tomography and its applications to biological tissues. *Optics Communications*, Vol.271, pp. 573-580

[24] Dubois, A.; Grieve, K.; Moneron, G.; Lecaque, R.; Vabre, L. & Boccara, A.C. (2004). Ultrahigh-resolution full-field optical coherence tomography. *Applied Optics*, Vol.43, pp. 2874-2882

[25] Dubois, A.; Moneron, G.; Grieve, K. & Boccara, A.C. (2004). Three-dimensional cellular-level imaging using full-field optical coherence tomography. *Physics in Medicine and Biology*, Vol.49, pp. 1227-1234

[26] Dubois, A.; Moreau, J. & Boccara, A.C. (2008). Spectroscopic ultrahigh-resolution full-field optical coherence microscopy. *Optics Express*, Vol.16, pp. 17082-17091

[27] Moneron, G.; Boccara, A.C. & Dubois, A. (2007). Polarization-sensitive full-field optical coherence tomography. *Optics Letters*, Vol.32, pp. 2058-2060

[28] Gale, D.M.; Pether M.I. & Dainty, J.C. (1996). Linnik microscope imaging of integrated circuit structures. *Applied Optics*, Vol.35, pp. 131-148

[29] Dubois, A.; Moneron, G. & Boccara, A.C. (2006). Thermal-light full-field optical coherence tomography in the 1.2 micron wavelength region. *Optics Communications*, Vol.266, pp. 738-743

[30] Oh, W.Y.; Bouma, B.E.; Iftimia, N.; Yun, S.H.; Yelin, R. & Tearney G.J. (2006). Ultrahigh-resolution full-field optical coherence microscopy using InGaAs camera. *Optics Express*, Vol.14, pp. 726-735

[31] Parsa, P.; Jacques, S.L. & Nishioka, N.S. (1989). Optical properties of rat liver between 350 and 2200 nm. *Applied Optics*, Vol. 28, pp. 2325-2330

[32] Schmitt, J.M.; Knuttel, A.; Yadlowsky, M. & Eckhaus, M.A. (1994). Optical coherence tomography of a dense tissue: statistics of attenuation and backscattering. *Physics in Medicine and Biology*, Vol.39, pp. 1705-1720

[33] Hale, G.M.; Querry, M.R. (1973). Optical constants of water in the 200 nm – 200 μm wavelength region. *Applied Optics,* Vol. 12, pp. 555-563

[34] Pan, Y. & Farkas D. L. (1998). Noninvasive imaging of living human skin with dual-wavelength optical coherence tomography in two and three dimensions. *Journal of Biomedical Optics*, Vol.3, pp. 446-455.

[35] Aguirre, A.D.; Nishizawa, N.; Seitz, W.; Ledere, M.; Kopf, D. & Fujimoto, J.G. (2006). Continuum generation in a novel photonic crystal fiber for ultrahigh resolution optical coherence tomography at 800 nm and 1300 nm. *Optics Express*, Vol.14, pp. 1145-1160

[36] Sacchet, D.; Moreau, J.; Georges, P. & Dubois, A. (2008). Simultaneous dual-band ultra-high resolution full-field optical coherence tomography. *Optics Express*, Vol.16, pp. 19434-19446

[37] Van Staveren, H.G.; Moes, C.J.M.; Van Marle, J.; Prahl, S.A. & Van Gemert, M.J.C. (1991). Light scattering in Intralipid-10% in the wavelength range of 400-1100 nanometers. *Applied Optics*, Vol.30, pp. 4507-4515

[38] Flock, S.T.; Jacques, S.L.; Wilson, B.C; Star, W.M. & Van Gemert, M.J.C. (1992). Optical properties of Intralipid: a phantom medium for light propagation studies. *Lasers in Surgery and Medicine,* Vol. 12, pp. 510-519

[39] Drexler, W.; Morgner, U.; Kärtner, F.X.; Pitris, C.; Boppart, S.A.; Li, X.D.; Ippen, E.P. & Fujimoto, J.G. (1999). In-vivo ultrahigh-resolution optical coherence tomography. *Optics Letters*, Vol. 24, pp. 1221-1223

[40] Wang, Y.; Zhao, Y.; Nelson, J.S.; Chen, Z. & Windeler, R.S. (2003). Ultrahigh-resolution optical coherence tomography by broadband continuum generation from a photonic crystal fiber. *Optics Letters,* Vol.28, pp. 182-184

[41] Alfidi, R. J.; MacIntyre, W. J. & Haaga, R. (1976). The effects of biological motion in CT resolution. *American Journal of Radiology*, Vol.127, pp. 11-15

[42] Wood, M.L. & Henkelman, R.M. (1985). NMR image artifact from periodic motion. *Medical Physics*, Vol.12, pp. 143-151

[43] Nadkarni, S.K.; Boughner, D.R.; Drangova, M. & Fenster, A. (2001). In vitro simulation and quantification of temporal jitter artifacts in ECG-gated dynamic three-dimensional echocardiography. *Ultrasound in Medicine & Biology*, Vol.27, pp. 211-222

[44] Yun, S.H.; Tearney, G.; De Boer, J. & Bouma, B. (2004). Motion artifacts in optical coherence tomography with frequency-domain ranging, *Optics Express*, Vol.12, pp. 2977-2998

[45] Sacchet, D.; Brzezinski, M.; Moreau, J.; Georges, P. & Dubois, A. (2010). Motion artifact suppression in full-field optical coherence tomography. *Applied Optics*, Vol.49, pp. 1480-1488

[46] Moneron, G.; Boccara, A.C & Dubois, A. (2005). Stroboscopic ultrahigh-resolution full-field optical coherence tomography, *Optics Letters*, Vol.30, pp. 1351-1353

[47] Grieve, K. ; Dubois, A. ; Simonutti, M. ; Pâques, M. ; Sahel, J. ; Le Gargasson, J.F. & Boccara A.C. (2005). In vivo anterior segment imaging in the rat eye with high speed white light full-field optical coherence tomography. *Optics Express*, Vol.13, pp. 6286-6295

[48] Hrebesh, M.S.; Dabu, R. & Sato, M. (2009). In vivo imaging of dynamic biological specimen by real-time single-shot full-field optical coherence tomography. *Optics Communications*, Vol.282, pp. 674-683

[49] Watanabe, Y. & Sato, M. (2008). Three-dimensional wide-field optical coherence tomography using an ultrahigh-speed CMOS camera. *Optics Communications*, Vol.281, pp. 1889-1895

[50] Akiba, M.; Chan, K.P. & Tanno, N. (2003). Full-field optical coherence tomography by two-dimensional heterodyne detection with a pair of CCD cameras. *Optics Letters*, Vol.28, pp. 816-818

[51] Grieve, K.; Paques, M.; Dubois, A.; Sahel, J.; Boccara, A.C. & Le Gargasson, J.F. (2004). Ocular tissue imaging using ultrahigh-resolution full-field optical coherence tomography. *Investigative Ophthalmology & Visual Science*, Vol.45, pp. 4126-413

[52] Boccara, M.; Schwartz, W.; Guiot, E.; Vidal, G.; De Paepe, R.; Dubois, A. & Boccara, A.C. (2007). Early chloroplastic alterations analysed by optical coherence tomography during harpin-induced hypersensitive response. *The Plant Journal*, Vol.50, pp. 338-346

[53] Perea-Gomez, A.; Moreau, A.; Camus, A.; Grieve, K.; Moneron, G.; Dubois, A.; Cibert, C. & Collignon, J. (2004). Initiation of gastrulation in the mouse embryo is preceded by an apparent shift in the orientation of the anterior-posterior axis. *Current Biology*, Vol.14, pp. 197-207
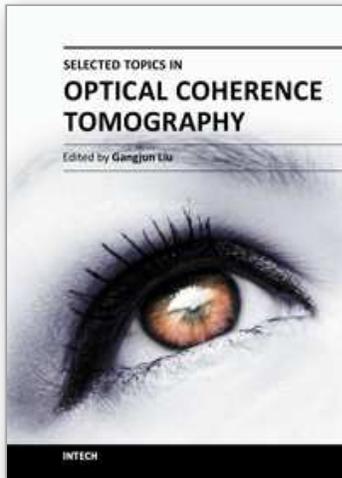
Selected Topics in Optical Coherence Tomography

Edited by Dr. Gangjun Liu

This book includes different exciting topics in the OCT fields, written by experts from all over the world. Technological developments, as well as clinical and industrial applications are covered. Some interesting topics like the ultrahigh resolution OCT, the functional extension of OCT and the full field OCT are reviewed, and the applications of OCT in ophthalmology, cardiology and dentistry are also addressed. I believe that a broad range of readers, such as students, researchers and physicians will benefit from this book.

How to reference

In order to correctly reference this scholarly work, feel free to copy and paste the following:

Arnaud Dubois (2012). Full-Field Optical Coherence Microscopy, Selected Topics in Optical Coherence Tomography, Dr. Gangjun Liu (Ed.), ISBN: 978-953-51-0034-8, InTech, Available from: http://www.intechopen.com/books/selected-topics-in-optical-coherence-tomography/full-field-optical-coherence-microscopy

INTECH
open science | open minds